# TRADE-OFF STUDY ON LARGE CONSTELLATION DE-ORBITING USING LOW-THRUST AND DE-ORBITING BALLOONS

**Simeng Huang,[*] Camilla Colombo,[†] and Elisa Maria Alessi[‡]**

This paper conducts a trade-off study on large constellation de-orbiting by using low-thrust and de-orbiting balloons. A novel de-orbiting strategy is proposed: the low-thrust propulsion is firstly used to actively de-orbit the satellites to de-orbiting corridors, and the de-orbiting balloons are then deployed to enhance the passive de-orbiting, driven by the resonances of natural perturbations. The study is conducted via two layers − the first layer is designing the low-thrust trajectories for a single satellite; the second layer is conducting the trade-off analysis for a large constellation. In the first layer, a near time-minimum steering law, which can directly be applied to each satellite from a constellation, is developed by using the theory of extrema; to reduce the computation load, the secular variations of the orbital elements are derived by using the orbital averaging technique. In the second layer, three figures of merit – coverage performance, fuel consumption, and total time to de-orbit − are discussed, and maps are drawn in colour as a function of constellation locations; by reading the maps, the trade-off analysis is conducted and a cost-efficiency approach is employed to identify the feasible constellation locations that fulfil various requirements.

## INTRODUCTION

Over the past years, the international interest in large constellations, which are aiming to provide high-speed telecommunication services, is increasingly growing. Many companies, such as OneWeb [1] and SpaceX [2], have announced their plans to deploy large constellations in Low Earth Orbit (LEO). However, the increase of large constellations, which are composed of hundreds to thousands of satellites, will pose a severe safety threat to the already congested LEO regime. To make the space sustainably usable, large constellations must be properly removed after their end of life. According to the plan of the OneWeb constellation, the low-thrust propulsion will be used to actively de-orbit the satellites to the drag dominated region [3].

With the development of materials and manufacturing technology, more and more passive de-orbiting devices (e.g. drag and solar sail, electrodynamic tether) have been considered for passive de-orbiting. Feasibility studies on de-orbiting balloons have been conducted, demonstrating that such devices can enhance the passive de-orbiting from high-altitude LEO, by ex-

[*] PhD Student, Department of Aerospace Science and Technology, Politecnico di Milano, Via Giuseppe La Masa 34, 20156 Milano, Italy, simeng.huang@polimi.it.
[†] Associate Professor, Department of Aerospace Science and Technology, Politecnico di Milano, Via Giuseppe La Masa 34, 20156 Milano, Italy, camilla.colombo@polimi.it.
[‡] Researcher, Istituto di Fisica Applicata "Nello Carrara" – Consiglio Nazionale delle Ricerche (IFAC-CNR), Via Madonna del Piano 10, 50019 Sesto Fiorentino, Italy, em.alessi@ifac.cnr.it.

ploiting dynamical resonances due to the coupled effect of Earth's oblateness and Solar Radiation Pressure (SRP). The eccentricity is passively increased by this phenomenon, given a high enough value of area-to-mass ratio [4-9].

Motivated by the previous works, this paper proposes a novel de-orbiting strategy with the potential application to large constellations, by using low-thrust propulsion and de-orbiting balloons. The proposed de-orbiting strategy is composed of two phases – active phase and passive phase. In the active phase, the low-thrust propulsion will be used to actively de-orbit a satellite to its targeted de-orbiting corridor. Once the targeted de-orbiting corridor is reached, the low-thrust propulsion system will be turned off, and the passive phase starts. In the passive phase, the de-orbiting balloon will be augmented to enhance the passive de-orbiting driven by the natural effects, until the drag dominated region is reached. Different from the traditional way in which the eccentricity is actively increased by the low-thrust, the eccentricity in the new strategy is passively increased by the natural effects, and the low-thrust will only be used to reach the de-orbiting corridors, thus consuming less fuel. A comparative study on the two de-orbiting strategies has been done in [10] for the large constellations deployed at high inclinations ($\geq 80$ deg), demonstrating the new strategy is advantageous to saving propellant.

The study is conducted via two layers: the first layer is the low-thrust trajectory design for a single satellite; the second layer is the trade-off analysis for a large constellation. For the first layer, considering the large number of satellites in large constellations, rather than using the direct or indirect method, it is expected to develop a general steering law that can directly be applied to every satellite from the constellation. Thanks to the fact that in the proposed de-orbiting strategy there is only one terminal condition – targeted de-orbiting corridor, it is possible to derive the local time-optimal steering law by using the theory of extrema, which has been used in many of the previous works, such as [11-13]. To further reduce the high computation load caused by the large number of satellites and low thrust-to-mass ratio, the optimal steering law will be simplified as a near optimal steering law, and the orbital averaging technique will be used to derive the secular variations of the orbital elements. In the second layer, three figures of merit are to be discussed: fuel consumption, total time to de-orbit, and constellation coverage performance. For each figure of merit, a map will be drawn in colour as a function of the constellation position, which is indicated by the constellation altitude and inclination, to identify the feasible region where the constellations can be placed.

It should be noticed that the major contribution of this work is the active phase, whereas for the passive phase, the theoretical research can be found in [7-9]. Besides, the study scope of this paper concerns the prograde orbits (i.e. $i \leq 90$ deg) in LEO regime (i.e. altitude lower than 2,000 km), in accordance with most of the plans of large constellations, such as OneWeb [1] and Starlink [2].

The remaining of this paper is organised as follows. In the first section, the first layer – low-thrust trajectory design for a single satellite – will be solved by developing a near time-optimal steering law and obtaining the secular variations of the orbital elements; the numerical validations will be presented to show the accuracy of the secular solutions. In the second section, the second layer – trade-off analysis for a large constellation – will be addressed by mapping three figures of merit as a function of the constellation position and conducting the trade-off analysis based on the maps.

## LOW-THRUST TRAJECTORY DESIGN FOR A SINGLE SATELLITE

This section will address the first layer of the study on the satellite level, designing the near time-optimal steering law and deriving the secular variations of the orbital elements.

### Dynamical Model

The dynamical model due to low-thrust can be given in the form of the rates of change of the orbital elements with respect to the eccentric anomaly [14]:

$$\frac{\mathrm{d}a}{\mathrm{d}E}=\frac{2a^3}{\mu}\left(e\sin E u_r+\sqrt{1-e^2}u_\theta\right) \tag{1}$$

$$\frac{\mathrm{d}e}{\mathrm{d}E}=\frac{a^2}{\mu}\left(\left(1-e^2\right)\sin E u_r+\sqrt{1-e^2}\left(2\cos E-e-e\cos^2 E\right)u_\theta\right) \tag{2}$$

$$\frac{\mathrm{d}i}{\mathrm{d}E}=\frac{a^2}{\mu}\left(\frac{\cos E-e}{\sqrt{1-e^2}}\cos\omega-\sin E\sin\omega\right)\left(1-e\cos E\right)u_h \tag{3}$$

$$\frac{\mathrm{d}\Omega}{\mathrm{d}E}=\frac{a^2}{\mu\sin i}\left(\frac{\cos E-e}{\sqrt{1-e^2}}\sin\omega+\sin E\cos\omega\right)\left(1-e\cos E\right)u_h \tag{4}$$

$$\frac{\mathrm{d}\omega}{\mathrm{d}E}=\frac{a^2}{\mu e}\left(\sqrt{1-e^2}\left(e-\cos E\right)u_r+\left(2-e^2-e\cos E\right)\sin E u_\theta\right)-\cos i\frac{\mathrm{d}\Omega}{\mathrm{d}E} \tag{5}$$

where, $\mu \approx 3.986 \times 10^5$ km$^3$/s$^2$ is the Earth's gravitational constant, $a$ is the semi-major axis, $e$ is the eccentricity, $i$ is the inclination, $\Omega$ is the right ascension of ascending node, $\omega$ is the argument of perigee, $E$ is the eccentric anomaly, $u_r$, $u_\theta$, and $u_h$ are the components of the low-thrust acceleration, along radial, transversal, and normal direction, respectively, given by

$$u_r = u_{\text{thrust}}\cos\beta\cos\alpha \tag{6}$$

$$u_\theta = u_{\text{thrust}}\cos\beta\sin\alpha \tag{7}$$

$$u_h = u_{\text{thrust}}\sin\beta \tag{8}$$

with $u_{\text{thrust}}$ being the magnitude of the low-thrust acceleration, $\alpha$ and $\beta$ being the in-plane and out-of-plane steering angle, respectively, as shown in Figure 1, referred to as pitch angle and yaw angle.

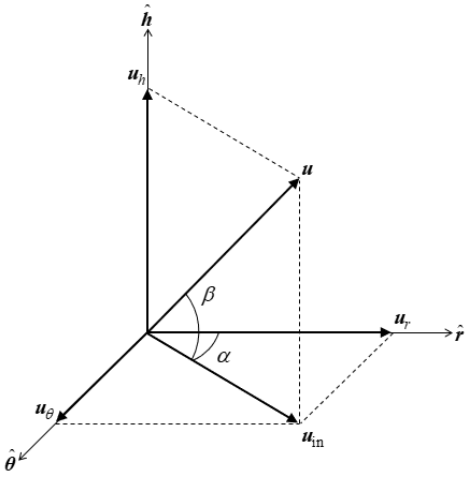


**Figure 1 Direction of the low-thrust acceleration.**

In the above model, the time rate of change of the eccentric anomaly, even though we are addressing a perturbed problem, has been approximated as the two-body problem:

$$\frac{\mathrm{d}E}{\mathrm{d}t}\approx\sqrt{\frac{\mu}{a^3}}\frac{1}{1-e\cos E} \tag{9}$$

due the fact that $u_{\text{thrust}}$ ($\leq 10^{-7}$ km/s$^2$) is far smaller than the magnitude of the gravitational acceleration ($\geq 10^{-4}$ km/s$^2$). $u_{\text{thrust}}$ is given by

$$u_{\text{thrust}} = \frac{2\eta P}{m g_0 I_{sp}} \tag{10}$$

where, $P$ is the engine input power, $\eta$ is the engine efficiency, $I_{sp}$ is the specific impulse, $g_0$ is the Earth's gravitational acceleration at the sea-level, and $m$ is the satellite mass, governed by

$$\frac{\mathrm{d}m}{\mathrm{d}t} = -m\frac{u_{\text{thrust}}}{g_0 I_{sp}} \tag{11}$$

The effects of Earth's shadow and $J_2$ perturbations are considered in this study. Regarding the Earth's shadow, the low-thrust is assumed to be turned off when the satellite is in shadow, and the entry and exit true anomalies of the Earth's shadow are obtained by solving a quartic equation [15]. Regarding the $J_2$ perturbations, the secular effects are considered [16]:

$$\frac{\mathrm{d}\bar{a}}{\mathrm{d}t}_{J_2} = \frac{\mathrm{d}\bar{e}}{\mathrm{d}t}_{J_2} = \frac{\mathrm{d}\bar{i}}{\mathrm{d}t}_{J_2} = 0 \tag{12}$$

$$\frac{\mathrm{d}\bar{\Omega}}{\mathrm{d}t}_{J_2} = -\frac{3}{2}\sqrt{\mu} J_2 R_E^2 a^{-\frac{7}{2}} \left(1-e^2\right)^{-2} \cos i \tag{13}$$

$$\frac{\mathrm{d}\bar{\omega}}{\mathrm{d}t}_{J_2} = \frac{3}{4}\sqrt{\mu} J_2 R_E^2 a^{-\frac{7}{2}} \left(1-e^2\right)^{-2} \left(5\cos^2 i - 1\right) \tag{14}$$

**Problem Statement**

There are in total six de-orbiting corridors [8]. Figure 2 shows the locations of the corridors as a function of $a$ and $i$ for $e = 10^{-3}$.

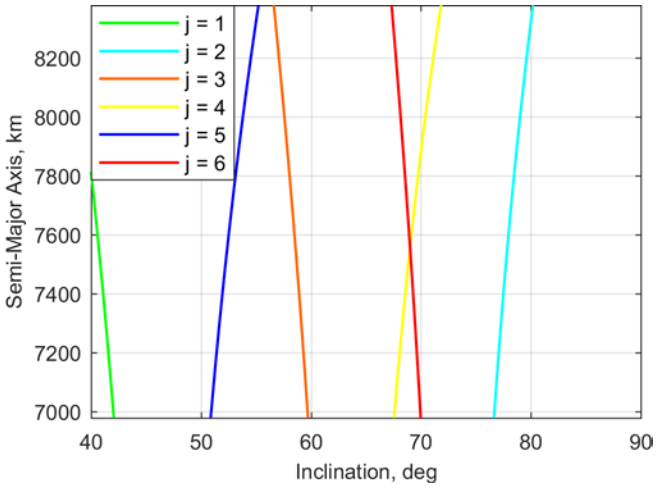


**Figure 2 Locations of the de-orbiting corridors ($e = 10^{-3}$).**

The terminal condition of the active phase is the targeted de-orbiting corridor, that is the corridor nearest to the satellite initial position, given by the mathematical expression of the locations of the corridors [8]:

$$n_1^* \frac{\mathrm{d}\bar{\Omega}}{\mathrm{d}t}_{J_2}\left(a_f, e_f, i_f\right) + n_2^* \frac{\mathrm{d}\bar{\omega}}{\mathrm{d}t}_{J_2}\left(a_f, e_f, i_f\right) + n_3^* n_S = 0 \tag{15}$$

where, the subscript $f$ indicates the final value of the orbital elements at the end of the active phase, the superscript * represents the targeted de-orbiting corridor, $n_S \approx 2\pi/365.25$ rad/day is the mean motion of the Sun measured on the ecliptic plane, and $n_1 = \{0, 1\}$, $n_2 = \pm 1$, and $n_3 = \pm 1$ are the parameters according to $j$, following Table 1.

**Table 1 De-orbiting in terms of $n_1$, $n_2$, $n_3$ [8]**

| $j$ | $n_1$ | $n_2$ | $n_3$ |
|---|---|---|---|
| 1 | 1 | 1 | −1 |
| 2 | 1 | −1 | −1 |
| 3 | 0 | 1 | −1 |
| 4 | 0 | 1 | 1 |
| 5 | 1 | 1 | 1 |
| 6 | 1 | −1 | 1 |

To identify the targeted de-orbiting corridor, let us first define $D$ as

$$D = n_1 \frac{\mathrm{d}\bar{\Omega}}{\mathrm{d}t}_{J_2}(a,e,i) + n_2 \frac{\mathrm{d}\bar{\omega}}{\mathrm{d}t}_{J_2}(a,e,i) + n_3 n_S \tag{16}$$

to quantitatively evaluate the instantaneous distance between the satellite and one of the six corridors. For a given satellite initial position, indicated by $a_0$, $e_0$, and $i_0$, by evaluating the absolute initial distance between the satellite and each corridor, we identify the de-orbiting corridor to be targeted as the one corresponding to the minimum absolute initial distance.

Take as example a satellite from the Starlink constellation with the initial position of $a_0$ = (1150 + $R_E$) km, $e_0$ = $10^{-3}$, and $i_0$ = 53 deg [17]. The initial distances are $D(j = 1) = -4.20\times10^{-7}$ rad/s, $D(j = 2) = -1.33\times10^{-6}$ rad/s, $D(j = 3) = 2.58\times10^{-7}$ rad/s, $D(j = 4) = 6.56\times10^{-7}$ rad/s, $D(j = 5) = -2.21\times10^{-8}$ rad/s, and $D(j = 6) = -9.36\times10^{-7}$ rad/s. The absolute value of $D(j = 5)$ is the minimum, implying that the fifth corridor is the nearest one to the satellite initial position. So, the targeted de-orbiting corridor is the fifth corridor. The graphical interpretation on the active phase is given in Figure 3, where the colour band represents the targeted de-orbiting corridor as a function of $a$ and $i$ for $e \leq 0.2$. As shown in the figure, the objective of the steering law design is to find the quickest paths for $a$, $e$, and $i$ to reach the targeted de-orbiting corridor.

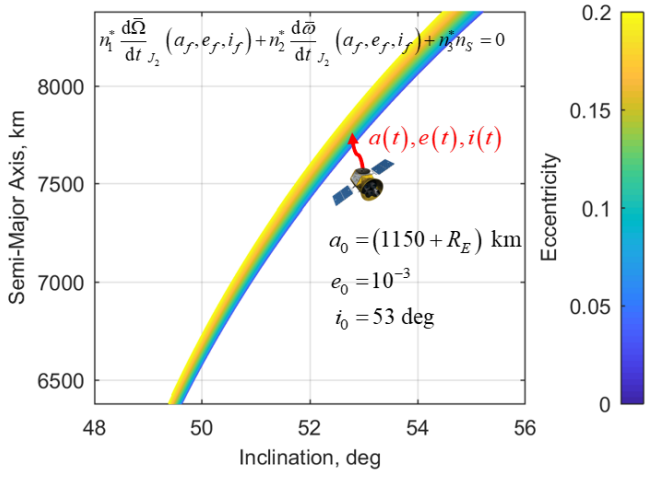


**Figure 3 Interpretation on the active phase for a satellite of the Starlink constellation.**

## Steering Law Design

The steering law design is divided into two steps: first choosing a proper in-plane steering law, and then designing the time-minimum out-of-plane steering law.

*In-Plane Steering Law.* The most efficient steering law to change the semi-major axis is tangential thrust [11], whereas in this study, transversal thrust – the thrust direction normal to the radial direction – is chosen for the following two reasons. Firstly, the efficiency of the transversal thrust to change the semi-major axis is almost the same as the tangential thrust for LEO orbits whose eccentricity is small ($e \leq 0.2$) [10].Secondly, the dynamical model by using transversal thrust is in simple fashion, making it easier to obtain the secular variations of the orbital elements, which will be presented in the next section.

*Out-of-Plane Steering Law.* Choosing transversal thrust as the in-plane steering law, the components of the thrust acceleration are given in the form of

$$u_r = 0 \tag{17}$$

$$u_\theta = u_{\text{thrust}} \cos\beta \tag{18}$$

$$u_h = u_{\text{thrust}} \sin\beta \tag{19}$$

Substituting (13) and (14) into Eq. (16), after some manipulations, the instantaneous distance between the satellite and targeted de-orbiting corridor can be written as

$$D^* = \frac{3\sqrt{\mu}J_2R_E^2}{4} a^{-\frac{7}{2}} \left(1-e^2\right)^{-2} \left(5n_2^* \cos^2 i - 2n_1^* \cos i - n_2^*\right) + n_3^* n_S \tag{20}$$

Taking the time derivative of $D^*$ gives

$$\frac{\mathrm{d}D^*}{\mathrm{d}t} = \frac{3\sqrt{\mu}J_2R_E^2}{8} \frac{\mathrm{d}E}{\mathrm{d}t} a^{-\frac{9}{2}} \left(1-e^2\right)^{-3} \begin{pmatrix} -7\left(1-e^2\right)\left(5n_2^* \cos^2 i - 2n_1^* \cos i - n_2^*\right)\dfrac{\mathrm{d}a}{\mathrm{d}E} \\ +8ae\left(5n_2^* \cos^2 i - 2n_1^* \cos i - n_2^*\right)\dfrac{\mathrm{d}e}{\mathrm{d}E} \\ +2a\left(1-e^2\right)\left(2n_1^* \sin i - 5n_2^* \sin 2i\right)\dfrac{\mathrm{d}i}{\mathrm{d}E} \end{pmatrix} \tag{21}$$

Then substituting Eqs. (1) – (3) into Eq. (21) and replacing with Eqs. (17) – (19), $\mathrm{d}D^*/\mathrm{d}t$ can be rewritten as

$$\frac{\mathrm{d}D^*}{\mathrm{d}t} = u_{\text{thrust}} \frac{3J_2R_E^2}{4\sqrt{\mu}} \frac{\mathrm{d}E}{\mathrm{d}t} a^{-\frac{3}{2}} \left(1-e^2\right)^{-\frac{5}{2}} \begin{pmatrix} \left(c_a\left(1-e^2\right) + c_e e\left(2\cos E - e - e\cos^2 E\right)\right)\cos\beta \\ +c_i\left(\left(\cos E - e\right)\cos\omega - \sqrt{1-e^2}\sin E \sin\omega\right)\left(1-e\cos E\right)\sin\beta \end{pmatrix} \tag{22}$$

where, $c_a$, $c_e$, and $c_i$ are functions of $i$, given by

$$c_a = -7\left(5n_2^* \cos^2 i - 2n_1^* \cos i - n_2^*\right) \tag{23}$$

$$c_e = 4\left(5n_2^* \cos^2 i - 2n_1^* \cos i - n_2^*\right) \tag{24}$$

$$c_i = 2n_1^* \sin i - 5n_2^* \sin 2i \tag{25}$$

To find the best yaw angle to change $D^*$, let us take the partial derivative of $\mathrm{d}D^*/\mathrm{d}t$ with respect to $\beta$ and solve for zero, then the local extrema solutions can be obtained:

$$\cos\beta = \text{sign}\left[-D_0^*\right] \frac{c_a\left(1-e^2\right) + c_e e\left(2\cos E - e - e\cos^2 E\right)}{\sqrt{\left(c_a\left(1-e^2\right) + c_e e\left(2\cos E - e - e\cos^2 E\right)\right)^2 + c_i^2\left(\left(\cos E - e\right)\cos\omega - \sqrt{1-e^2}\sin E\sin\omega\right)^2\left(1-e\cos E\right)^2}} \tag{26}$$

$$\sin\beta = \operatorname{sign}\left[-D_0^*\right]\frac{c_i\left(\left(\cos E - e\right)\cos\omega - \sqrt{1-e^2}\,\sin E\sin\omega\right)\left(1-e\cos E\right)}{\sqrt{\left(c_a\left(1-e^2\right)+c_e e\left(2\cos E - e - e\cos^2 E\right)\right)^2 + c_i^2\left(\left(\cos E - e\right)\cos\omega - \sqrt{1-e^2}\,\sin E\sin\omega\right)^2\left(1-e\cos E\right)^2}} \tag{27}$$

where, $D_0^*$ is the initial distance between the satellite and targeted de-orbiting corridor, the symbol sign[▫] represents the sign of the generic variable ▫; if $D_0^* > 0$, then sign[$-D_0^*$] = −1, indicating the local minima solutions, whereas if $D_0^* < 0$, then sign[$-D_0^*$] = +1, indicating the local maxima solutions.

If we check a priori, we can find that the final eccentricity is always less than 0.1, because the transversal thrust is not efficient to change the eccentricity. Therefore, it is enough to neglect the eccentricity, and hence we can get the near optimal out-of-plane steering law

$$\cos\beta = \operatorname{sign}\left[-D_0^*\right]\frac{c_a}{\sqrt{c_a^2 + c_i^2\cos^2\left(\omega+E\right)}} \tag{28}$$

$$\sin\beta = \operatorname{sign}\left[-D_0^*\right]\frac{c_i\cos\left(\omega+E\right)}{\sqrt{c_a^2 + c_i^2\cos^2\left(\omega+E\right)}} \tag{29}$$

Finally, substituting Eqs. (17) − (19) into Eqs. (1) − (5) and replacing with Eqs. (28) and (29), the dynamical model due to the near optimal steering laws is given by

$$\frac{\mathrm{d}a}{\mathrm{d}E} = \operatorname{sign}\left[-D_0^*\right]u_{\text{thrust}}\frac{2c_a a^3\sqrt{1-e^2}}{\mu}\frac{1}{\sqrt{c_a^2 + c_i^2\cos^2\left(\omega+E\right)}} \tag{30}$$

$$\frac{\mathrm{d}e}{\mathrm{d}E} = \operatorname{sign}\left[-D_0^*\right]u_{\text{thrust}}\frac{c_a a^2\sqrt{1-e^2}}{\mu}\frac{2\cos E - e - e\cos^2 E}{\sqrt{c_a^2 + c_i^2\cos^2\left(\omega+E\right)}} \tag{31}$$

$$\frac{\mathrm{d}i}{\mathrm{d}E} = \operatorname{sign}\left[-D_0^*\right]u_{\text{thrust}}\frac{c_i a^2}{\mu}\left(\frac{\cos E - e}{\sqrt{1-e^2}}\cos\omega - \sin E\sin\omega\right)\frac{\left(1-e\cos E\right)\cos\left(\omega+E\right)}{\sqrt{c_a^2 + c_i^2\cos^2\left(\omega+E\right)}} \tag{32}$$

$$\frac{\mathrm{d}\Omega}{\mathrm{d}E} = \operatorname{sign}\left[-D_0^*\right]u_{\text{thrust}}\frac{c_i a^2}{\mu\sin i}\left(\frac{\cos E - e}{\sqrt{1-e^2}}\sin\omega + \sin E\cos\omega\right)\frac{\left(1-e\cos E\right)\cos\left(\omega+E\right)}{\sqrt{c_a^2 + c_i^2\cos^2\left(\omega+E\right)}} \tag{33}$$

$$\frac{\mathrm{d}\omega}{\mathrm{d}E} = \operatorname{sign}\left[-D_0^*\right]u_{\text{thrust}}\frac{c_a a^2}{\mu e}\frac{\left(2-e^2-e\cos E\right)\sin E}{\sqrt{c_a^2 + c_i^2\cos^2\left(\omega+E\right)}} - \cos i\frac{\mathrm{d}\Omega}{\mathrm{d}E} \tag{34}$$

**Secular Rates of Change of Orbital Elements**

Due to the low thrust-to-mass ratio, the low-thrust trajectories usually consist of hundreds to thousands of revolutions and the transfer time can be several months or even up to few years. Therefore, the full dynamics integration is computationally consuming, let alone the computation for hundreds to thousands of satellites in large constellations. To reduce the high computation load, an orbital averaging technique is used to derive the secular variations of the orbital elements by integrating in the eccentric anomaly, under the assumption that all orbital elements except the eccentric anomaly are constant over one revolution. Here, let $x$ denote one of the five orbital elements to be averaged (i.e. $x$ can be either $a$, $e$, $i$, Ω, or $\omega$) and let fun$^x$ denote the primitive function of the indefinite integral of d$x$/d$E$.

Unfortunately, Eqs. (30) – (34) cannot be integrated analytically. However, observing that $cos(\omega + E)$ is periodic, let us expand the term $(c_a^2 + c_i^2\cos^2(\omega + E))^{-1/2}$ in Fourier series before doing the integration:

$$\frac{1}{\sqrt{c_a^2 + c_i^2\cos^2(\omega+E)}} \approx \frac{2}{\pi\sqrt{c_a^2 + c_i^2}}\sum_{k=0}^{4} f_k \cos\left(2k(\omega+E)\right) \tag{35}$$

where, $f_k$ ($k$ = 0 to 4) are the Fourier series coefficients; $f_k$ can be written in the form of

$$f_k = f_k^F \text{elliptic}F[\rho] + f_k^E \text{elliptic}E[\rho] \tag{36}$$

where, $f_k^F$ and $f_k^E$ are functions of $c_a$ and $c_i$, seen in Appendix-A, elliptic$F$ and elliptic$E$ are the complete elliptic integrals of the first and second kinds, given by [16]

$$\text{elliptic}F[\rho] = \int_0^{\pi/2} \frac{1}{\sqrt{1-\rho\sin^2\varphi}}\mathrm{d}\varphi \tag{37}$$

$$\text{elliptic}E[\rho] = \int_0^{\pi/2} \sqrt{1-\rho\sin^2\varphi}\,\mathrm{d}\varphi \tag{38}$$

with the modulus $\rho$ being

$$\rho = \frac{c_i^2}{c_a^2 + c_i^2} \tag{39}$$

Now substituting Eq. (35) into Eqs. (30) – (34) and integrating, the primitive functions can be obtained, and after considerable manipulations, given in the form of

$$\text{fun}^a = \text{sign}\left[-D_0^*\right]u_{\text{thrust}}\frac{4a^3\sqrt{1-e^2}}{\mu}\frac{c_a}{\pi\sqrt{c_a^2 + c_i^2}}\left(\sum_{k=0}^{4} f_k \text{fun}_k^a\right) \tag{40}$$

$$\text{fun}^e = \text{sign}\left[-D_0^*\right]u_{\text{thrust}}\frac{2a^2\sqrt{1-e^2}}{\mu}\frac{c_a}{\pi\sqrt{c_a^2 + c_i^2}}\left(\sum_{k=0}^{4} f_k \text{fun}_k^e\right) \tag{41}$$

$$\text{fun}^i = \text{sign}\left[-D_0^*\right]u_{\text{thrust}}\frac{2a^2}{\mu}\frac{c_i}{\pi\sqrt{c_a^2 + c_i^2}}\left(\sum_{k=0}^{4} f_k \text{fun}_k^i\right) \tag{42}$$

$$\text{fun}^\Omega = \text{sign}\left[-D_0^*\right]u_{\text{thrust}}\frac{2a^2}{\mu\sin i}\frac{c_i}{\pi\sqrt{c_a^2 + c_i^2}}\left(\sum_{k=0}^{4} f_k \text{fun}_k^\Omega\right) \tag{43}$$

$$\text{fun}^\omega = \text{sign}\left[-D_0^*\right]u_{\text{thrust}}\frac{2a^2}{\mu e}\frac{c_a}{\pi\sqrt{c_a^2 + c_i^2}}\left(\sum_{k=0}^{4} f_k \text{fun}_k^\omega\right) - \cos i\,\text{fun}^\Omega \tag{44}$$

where $\text{fun}_k^x$ ($k$ = 0 to 4) are functions of $e$, $\omega$, and $E$, seen in Appendix-B.

Taking the Earth's shadow into consideration, $\text{fun}^x$ should be evaluated between $E_{\text{ex}}$ and $E_{\text{en}}$, the exit and entry eccentric anomalies of the Earth's shadow, and hence the variation in $x$ over one revolution is given as

$$\Delta x_{\text{thrust}} = \begin{cases} \left[\text{fun}^x\right]_0^{E_{\text{en}}} + \left[\text{fun}^x\right]_{E_{\text{ex}}}^{2\pi} & \text{, if } E_{\text{en}} < E_{\text{ex}} \\ \left[\text{fun}^x\right]_{E_{\text{ex}}}^{E_{\text{en}}} & \text{, if } E_{\text{en}} > E_{\text{ex}} \end{cases} \tag{45}$$

Then, dividing by the Keplerian orbital period $T = 2\pi/n$, where $n = (\mu/a^3)^{1/2}$ is the mean motion in the two-body problem, the secular variation of $x$ due to low thrust can be obtained by the means of

$$\left(\frac{\mathrm{d}\overline{x}}{\mathrm{d}t}\right)_{\text{thrust}} = n\frac{\Delta x_{\text{thrust}}}{2\pi} \tag{46}$$

Finally, adding the secular effects of $J_2$ perturbations, the total secular variation of $x$ can be obtained:

$$\frac{\mathrm{d}\overline{x}}{\mathrm{d}t} = \left(\frac{\mathrm{d}\overline{x}}{\mathrm{d}t}\right)_{\text{thrust}} + \left(\frac{\mathrm{d}\overline{x}}{\mathrm{d}t}\right)_{J_2} \tag{47}$$

Regarding the satellite mass, the secular variation of $m$ is given by

$$\frac{\mathrm{d}\overline{m}}{\mathrm{d}t} = n\frac{\Delta m}{2\pi} \tag{48}$$

where $\Delta m$ is the mass loss over one revolution, given by

$$\left.\begin{aligned} \Delta m &= -\frac{2\eta P}{g_0^2 I_{sp}^2}\frac{1}{n}\left(M_{\text{en}} - M_{\text{ex}} + 2\pi\right) \quad ,\text{if } E_{\text{en}} < E_{\text{ex}} \\ \Delta m &= -\frac{2\eta P}{g_0^2 I_{sp}^2}\frac{1}{n}\left(M_{\text{en}} - M_{\text{ex}}\right) \qquad ,\text{if } E_{\text{en}} > E_{\text{ex}} \end{aligned}\right\} \tag{49}$$

with the mean anomalies $M_{\text{ex}}$ and $M_{\text{en}}$ being

$$\begin{aligned} M_{\text{ex}} &= E_{\text{ex}} - e\sin E_{\text{ex}} \\ M_{\text{en}} &= E_{\text{en}} - e\sin E_{\text{en}} \end{aligned} \tag{50}$$

**Numerical Validations**

A test transfer for the satellite from the Starlink constellation is solved to validate the accuracy of the secular variations of the orbital elements. The initial semi-major axis and inclination are $a_0 = (1150 + R_E)$ km and $i_0 = 53$ deg, respectively. The targeted de-orbiting corridor is the fifth corridor. The other mission scenarios are fixed as follows.

1) The effects of Earth's shadow and $J_2$ perturbations are included.
2) The start date of the de-orbiting, which is required for the Earth's shadow computation, is 1st of May, 2029.
3) The thrust engine parameters are $P = 200$ W, $I_{sp} = 1500$ s, $\eta = 50\%$, and the initial spacecraft mass is $m_0 = 150$ kg, resulting in a very small initial low-thrust acceleration of $9.06 \times 10^{-8}$ km/s$^2$.
4) The initial eccentricity is set as $e_0 = 10^{-3}$ to avoid the singularity during the integration of $\mathrm{d}\omega/\mathrm{d}E$, and the initial right ascension of ascending node, argument of perigee, and eccentric anomaly are arbitrarily given as $\Omega_0 = 0$ rad, $\omega_0 = 1$ rad, and $E_0 = 2$ rad, respectively.
5) The simulation stops if the targeted de-orbiting corridor is reached or the drag dominated, which is below the perigee altitude of 200 km, is reached.

Figure 4 compares the time histories of the orbital elements by full and secular dynamics integration for the two test transfers. It can be seen that the orbital elements have been averaged by using the orbital averaging technique and the secular dynamics integration shows good agreement with the full dynamics integration; the error in the argument of perigee is caused by the small eccentricity at the beginning of the transfer.

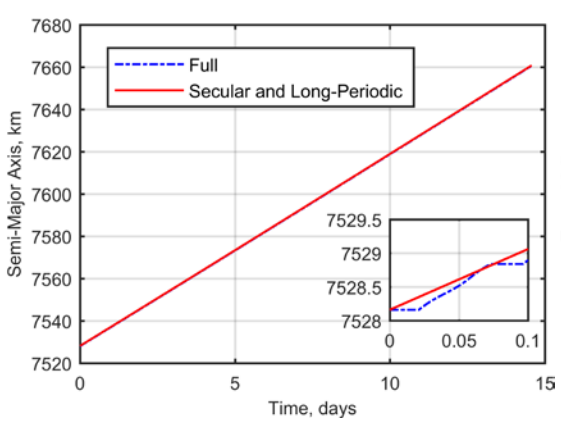


**a) Semi-major axis.**

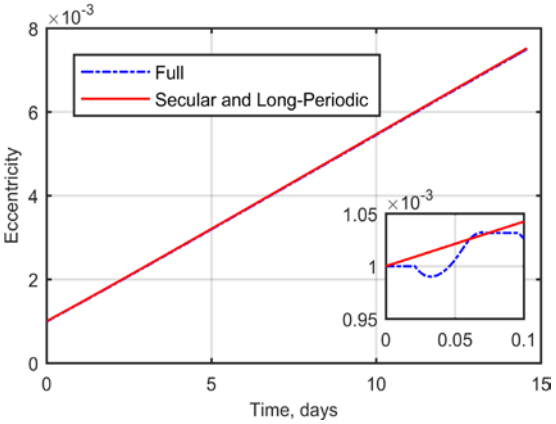


**b) Eccentricity.**

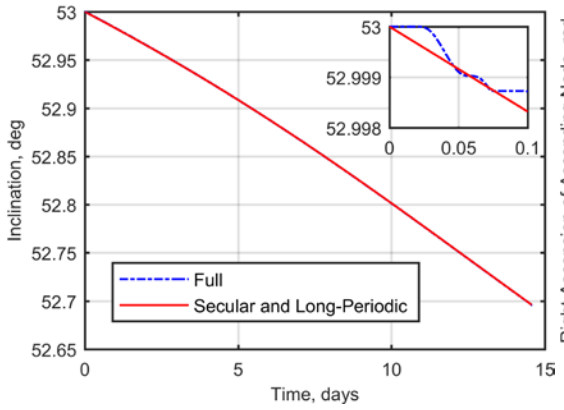


**c) Inclination.**

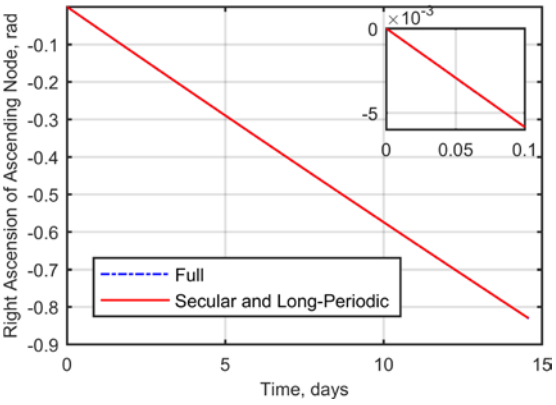


**d) Right ascension of ascending node.**

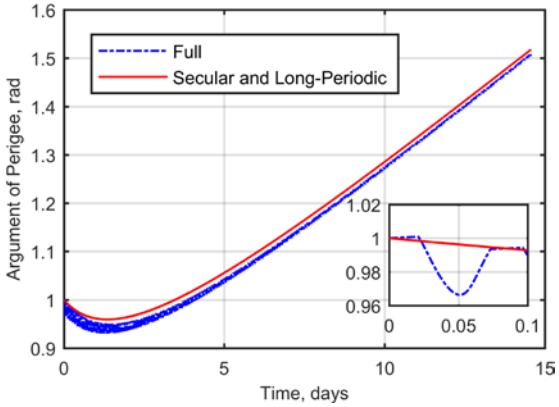


**d) Argument of perigee.**

**Figure 4 Comparison of the time histories of the orbital elements (Starlink).**

Table 2 compares the final results as well as the computation time by full and secular dynamics integration for the two test transfers. It can be seen that the secular dynamics integration is of high accuracy and can reduce the computation time by more than 50%.

**Table 2 Comparison of the final results (Starlink)**

| Integration | $a_f$, km | $e_f$ | $i_f$, deg | $\Omega_f$, rad | $\omega_f$, rad | $t_f$, days | Computation time, s |
|---|---|---|---|---|---|---|---|
| Full | 7660.71 | $7.49 \times 10^{-3}$ | 52.70 | −0.83 | 1.51 | 14.59 | 12.86 |
| Secular | 7660.78 | $7.52 \times 10^{-3}$ | 52.70 | −0.83 | 1.52 | 14.57 | 5.81 |

## TRADE-OFF ANALYSIS FOR A LARGE CONSTELLATION

This section will address the second layer at the constellation level. In this study, three figures of merit that are relevant to the system costs – coverage performance, fuel consumption, and total time to de-orbit – are to be discussed. For each figure of merit, a map will be drawn in colour as a function of constellation location indicated by the constellation initial altitude ($a_0 - R_E$) and constellation initial inclination $i_0$. By reading the maps, a trade-off analysis will be conducted, helping to identify the feasible constellation locations that meet various requirements.

It is of note that the results of the fuel consumption and total time to de-orbit presented in this section are for a single satellite. However, due to the fact that in most cases the semi-major axis, eccentricity, and inclination are identical for all satellites from the constellation, the targeted de-orbiting corridor, which is a function of $a$, $e$, and $i$, is also the same for all satellites from the constellation, and hence the results for a single satellite can be applied to the whole constellation.

### Figures of Merit

*Constellation Coverage Performance.* As the original motive that constellations were created, coverage is one of the prime cost drivers to assess the performance of a constellation [18]. In this study, the minimum ground elevation angle $\varepsilon_{\min}$ is used to quantitatively assess the coverage performance; for a given altitude, the larger the value of $\varepsilon_{\min}$, the better the coverage performance it will be [19]. Most of the large constellations are designed to provide continuous global coverage, whereas in this study, the continuous mid-latitude coverage, which covers the middle latitude regions between 0 and 60 deg north and south, is also considered, because these regions are heavily populated and hence the services provided to these regions satisfy most of the world's users [20].

Figure 5 a) and b) present in colour the best coverage performance that can be provided by a constellation of 1600 satellites and 32 orbital planes for continuous global and mid-latitude coverage, respectively. The regions with the white background indicate that the continuous global/mid-latitude coverage can not be provided if the constellation is deployed at such locations.

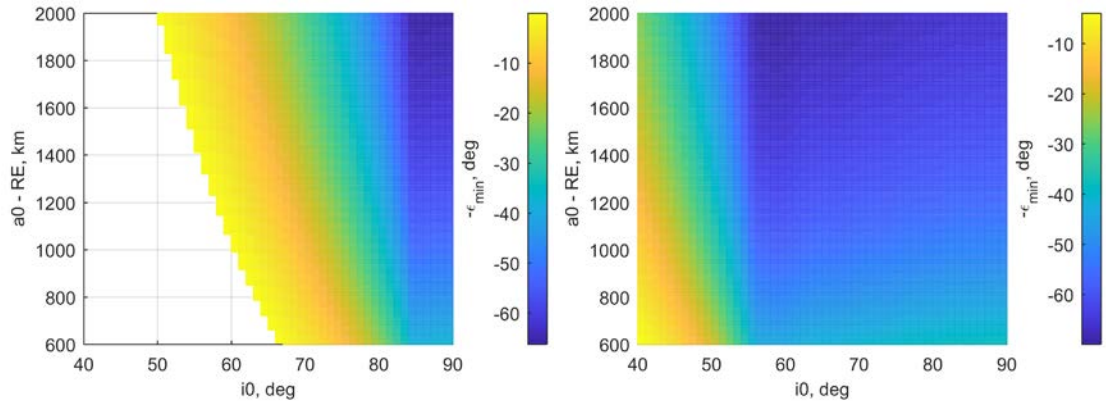


**a) Continuous global coverage.** **b) Continuous mid-latitude coverage.**

**Figure 5 Best coverage performance (1600 satellites, 32 orbital planes).**

It can be seen from the maps that: (1) for both continuous global and mid-latitude coverage, the coverage performance can be improved by deploying the constellation at high altitude; (2) for continuous global coverage, the coverage performance is benefited by high incli-

nation, whereas for continuous mid-latitude coverage, the coverage performance is benefited by middle inclination.

*Fuel Consumption.* The fuel consumption refers to the propellant used in the active phase to reach the de-orbiting corridors. Figure 6 presents in colour the fuel consumption $\Delta m_p$ for a single satellite.

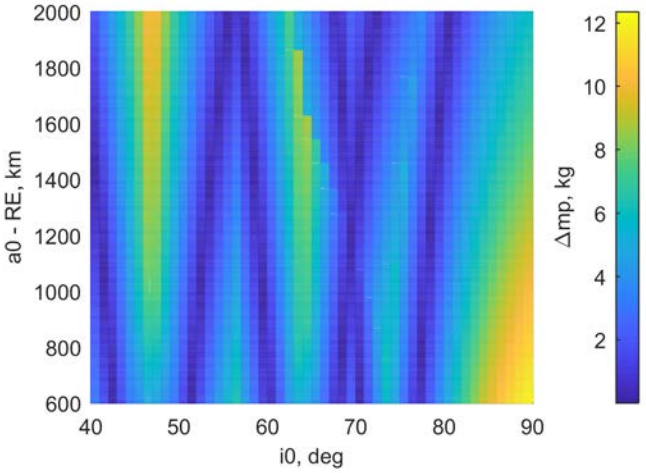


**Figure 6 Fuel consumption for a single satellite ($e_0 = 10^{-3}$).**

It can be seen from the map that: compared with the locations of de-orbiting corridors (Figure 2), the propellant can be saved by deploying the constellation nearer to the de-orbiting corridors.

*Total Time to De-Orbit.* The total time to de-orbit takes into account the time durations of the active and passive phases. The orbital propagator applied for the passive phase is the one developed for the ReDSHIFT software tool [21][22][23]. It considers the effects of Earth's zonal harmonics up to degree 5, of SRP within the assumptions of the cannonball model, of lunisolar perturbations, and of the atmospheric drag assuming the Jacchia-Roberts atmospheric density model with an exospheric temperature of 1000 K and a variable solar flux at 2800 MHz. The simulation stops if the drag dominated region, which is below the altitude of 200 km, is reached. The maximum time is 25 years, complying with the international regulation.

Figure 7 a) – d) present in colour the total time to de-orbit for a single satellite by using de-orbiting balloons with different area-to-mass ratios *A*/*m*. The regions with white background indicate that the constellation can not re-enter within 25 years if deployed at such locations.

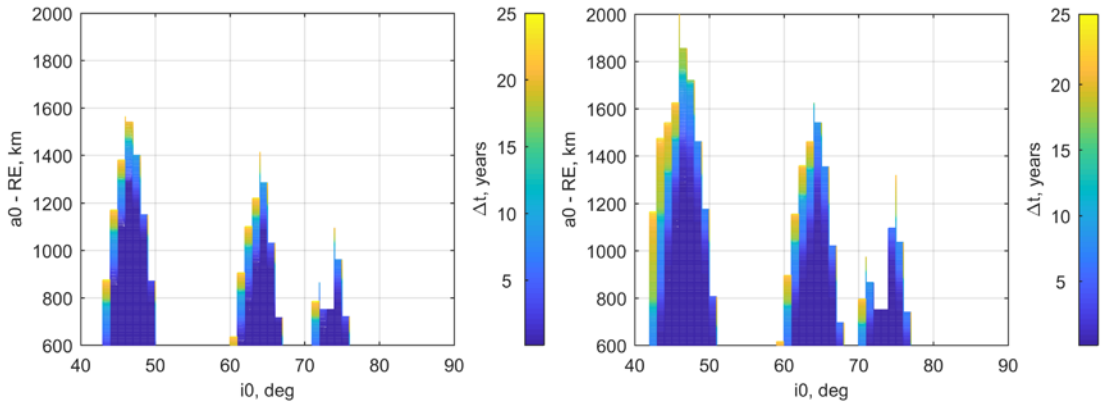


**a) $A/m$ = 0.01 m²/kg.** **b) $A/m$ = 0.1 m²/kg.**

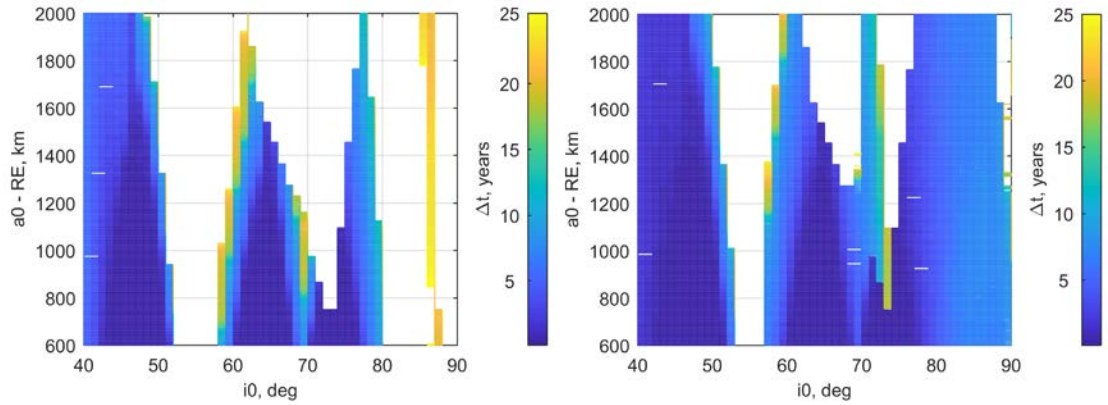


**c) $A/m$ = 1 m$^2$/kg.** **d) $A/m$ = 3 m$^2$/kg.**

**Figure 7 Total time to de-orbit of a single satellite ($e_0 = 10^{-3}$).**

It can be seen from the maps that: (1) the powerful regions leading to rapid re-entry are generally at the inclination of 40 − 50 deg, 60 − 70 deg, and 70 − 80 deg; (2) at the altitude between 1200 and 1400 km, which is the plan of most of the large constellations, it is possible to de-orbit the constellations within less than 10 years.

It should be stressed that at the polar inclination, there do not exist de-orbiting corridors, and the re-entry can not be achieved by only using the passive de-orbiting devices. However, with the proposed de-orbiting strategy (low-thrust combined with de-orbiting balloons), the satellites can be de-orbited within 25 years for there and also for high altitude, given the area-to-mass ratio higher than 1 kg/m$^2$.

## Trade-Off Analysis

Table 3 summarises the trade-offs between the three figures of merit in terms of the constellation locations. In the table, the up and down arrow indicate that the figures of merit can be improved by increasing and decreasing, respectively, the value of ($a_0 - R_E$) or $i_0$.

**Table 3 Summary of the figures of merit**

| Figure of merit | $a_0 - R_E$ | $i_0$ |
|---|---|---|
| Fuel consumption | Around de-orbiting corridors | |
| Total time to de-orbit | ↓ | 40 – 50 deg,<br>50 – 60 deg,<br>60 – 70 deg |
| Continuous global coverage performance | ↑ | ↑ |
| Continuous mid-latitude coverage performance | ↑ | Middle |

As the application of the maps, here we present a cost-efficiency approach to identify the constellation locations that meet the following requirements: (1) the minimum ground elevation angle is higher than 20 deg; (2) the fuel consumption for a single satellite is less than 2 kg; (3) the constellation can re-enter within 25 years.

In Figure 8, the regions on the right of the black dash line indicate the constellation locations fulfilling the coverage requirement. In Figure 9, the regions enclosed by the red solid line indicate the constellation locations fulfilling the fuel requirement.

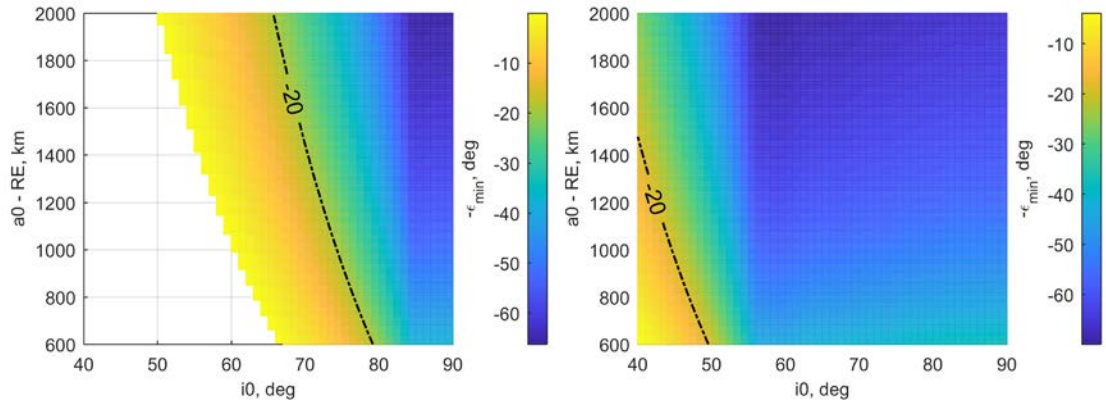


**a) Continuous global coverage.** **b) Continuous mid-latitude coverage.**

**Figure 8 Constellation locations fulfilling coverage requirement (1600 satellites, 32 orbital planes).**

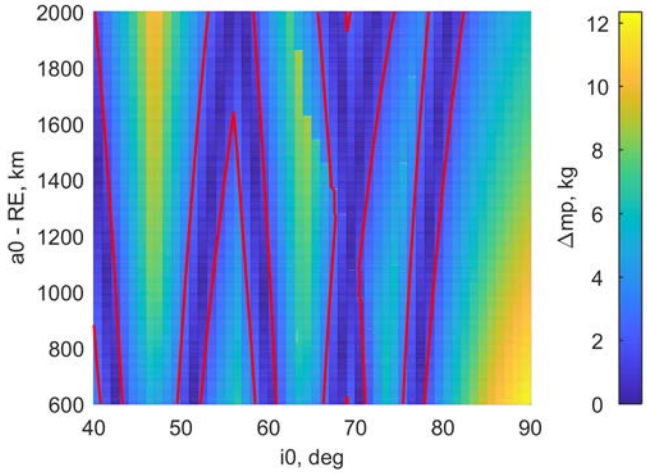


**Figure 9 Constellation locations fulfilling fuel requirement ($e_0 = 10^{-3}$).**

By merging Figure 8 and Figure 9 with Figure 7, the constellation locations that meet all requirements can be identified, as shown in Figure 10 and Figure 11 for global and mid-latitude coverage, respectively, in terms of different de-orbiting balloon area-to-mass ratios.

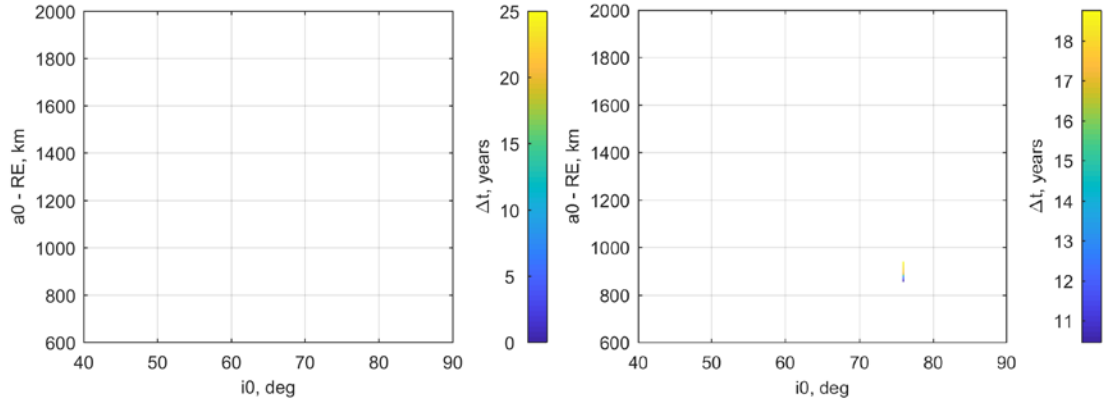


**a) $A/m$ = 0.01 m$^2$/kg.** **b) $A/m$ = 0.1 m$^2$/kg.**

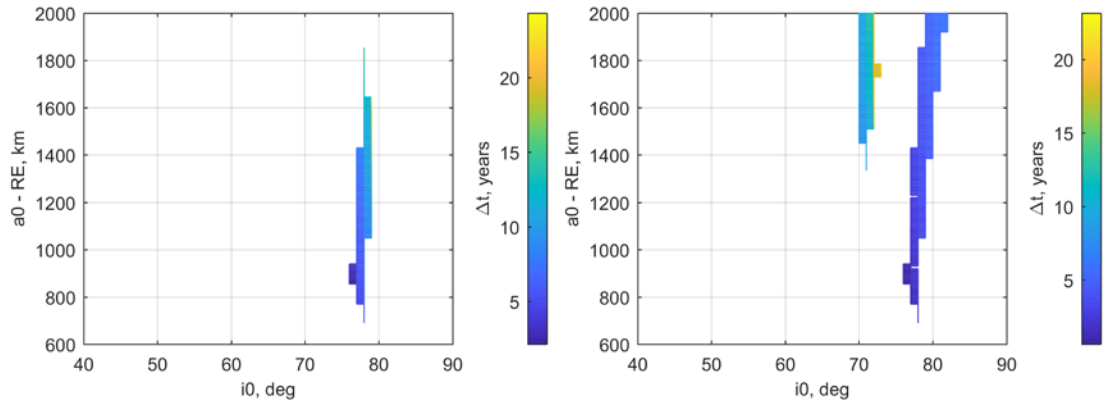


**c) $A/m$ = 1 m$^2$/kg.** **d) $A/m$ = 3 m$^2$/kg.**

**Figure 10 Constellation locations meeting all requirements for continuous global coverage ($e_0$ = $10^{-3}$, 1600 satellites, 32 orbital planes).**

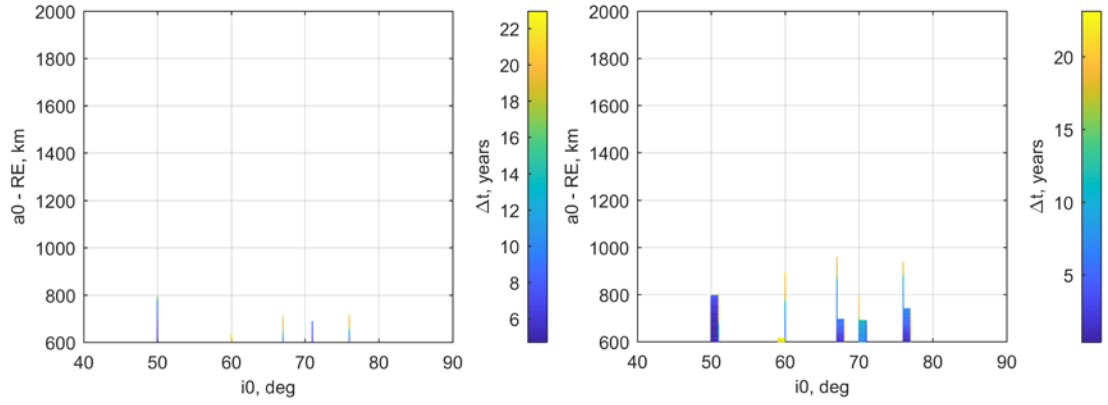


**a) $A/m$ = 0.01 m$^2$/kg.** **b) $A/m$ = 0.1 m$^2$/kg.**

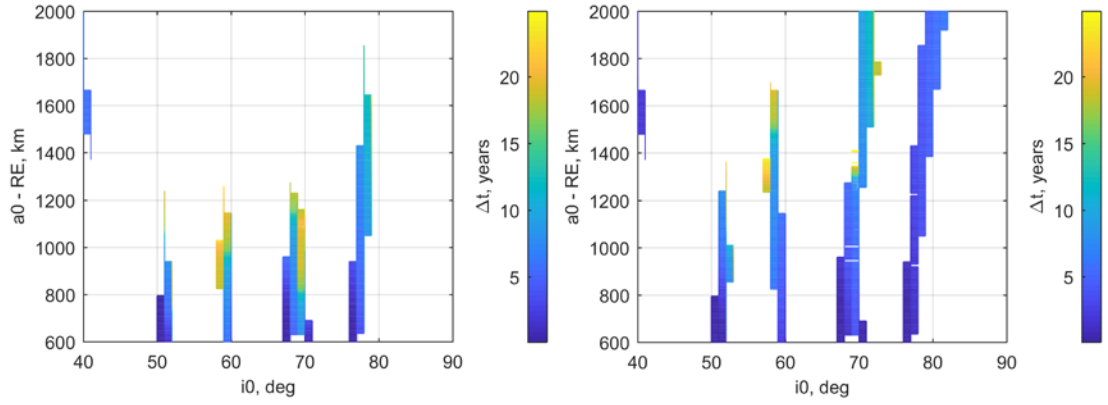


**c) $A/m$ = 1 m$^2$/kg.** **d) $A/m$ = 3 m$^2$/kg.**

**Figure 11 Constellation locations meeting all requirements for continuous mid-latitude coverage ($e_0$ = $10^{-3}$, 1600 satellites, 32 orbital planes).**

## CONCLUSION

This paper has conducted a trade-off study on large constellation de-orbiting by using low-thrust and de-orbiting balloons. A novel de-orbiting strategy has been proposed. The satellites are firstly actively de-orbited to the targeted de-orbiting corridor by using the low-thrust propulsion and then passively re-enter under the coupled effect of Earth's oblateness and SRP

with the aid of de-orbiting balloons. The study has been conducted via two layers: the first layer is designing the low-thrust trajectories for a single satellite; the second layer is conducting the trade-off analysis for a large constellation.

In the first layer, the near time-optimal steering law has been developed and the secular variations of the orbital elements have been derived. Regarding the steering law, it has been designed via two steps. The first step is choosing the transversal thrust as the in-plane steering law for its high efficiency to change the semi-major axis and simple fashion. The second step is deriving the local time-optimal out-of-plane steering law by using the theory of extrema, and after omitting the eccentricity, obtaining the near optimal steering law. The secular variations of the orbital elements have been derived by using the orbital averaging technique. A Fourier series expansion has been carried out before the integration. The numerical validations demonstrate that the secular dynamics integration has good agreement with the full dynamics integration and can reduce the computation time by more than 50%.

In the second layer, three figures of merit – fuel consumption, total time to de-orbit, and constellation coverage performance – have been discussed and the maps have been drawn in colour as a function of constellation locations that are indicated by constellation initial altitude and inclination. The maps show that there are trade-offs between the figures of merit in terms of the constellation locations. In the end, as an application of the maps, a cost-effectiveness approach has been presented to identify the feasible constellation position that meet all requirements.


## ACKNOWLEDGMENTS

The research leading to these results has received funding from the European Research Council (ERC) under the European Union's Horizon 2020 research and innovation programme as part of project COMPASS (Grant agreement No 679086).


## APPENDIX-A

Here present the expressions of $f_k^F$ and $f_k^E$ ($k$ = 0 to 4).

$$f_0^F = \tag{51}$$

$$f_0^E = \tag{52}$$

$$f_1^F = -\frac{2}{c_i^2}\left(2c_a^2 + c_i^2\right) \tag{53}$$

$$f_1^E = \frac{4}{c_i^2}\left(c_a^2 + c_i^2\right) \tag{54}$$

$$f_2^F = \frac{2}{3c_i^4}\left(16c_a^4 + 16c_a^2c_i^2 + 3c_i^4\right) \tag{55}$$

$$f_2^E = -\frac{16}{3c_i^4}\left(2c_a^4 + 3c_a^2c_i^2 + c_i^4\right) \tag{56}$$

$$f_3^F = -\frac{2}{15c_i^6}\left(256c_a^6 + 384c_a^4c_i^2 + 158c_a^2c_i^4 + 15c_i^6\right) \tag{57}$$

$$f_3^E = \frac{4}{15c_i^6}\left(128c_a^6 + 256c_a^4c_i^2 + 151c_a^2c_i^4 + 23c_i^6\right) \tag{58}$$

$$f_4^F = \frac{2}{105c_i^8}\left(6144c_a^8 + 12288c_a^6c_i^2 + 8000c_a^4c_i^4 + 1856c_a^2c_i^6 + 105c_i^8\right) \tag{59}$$

$$f_4^E = -\frac{64}{105c_i^8}\left(192c_a^8 + 480ca^6ci^2 + 406c_a^4c_i^4 + 129c_a^2c_i^6 + 11c_i^8\right) \tag{60}$$

**APPENDIX-B**

Here present the expressions of $\text{fun}_k^x$ ($k$ = 0 to 4), where $x$ denotes the orbital element $a$, $e$, $i$, Ω, or $\omega$.

$$\text{fun}_0^a = E \tag{61}$$

$$\text{fun}_1^a = \frac{1}{2}\sin(2\omega + 2E) \tag{62}$$

$$\text{fun}_2^a = \frac{1}{4}\sin(4\omega + 4E) \tag{63}$$

$$\text{fun}_3^a = \frac{1}{6}\sin(6\omega + 6E) \tag{64}$$

$$\text{fun}_4^a = \frac{1}{8}\sin(8\omega + 8E) \tag{65}$$

$$\text{fun}_0^e = \frac{1}{4}(8\sin E - e\sin 2E - 6eE) \tag{66}$$

$$\text{fun}_1^e = \frac{1}{48}\left(48\sin(2\omega + E) - 36e\sin(2\omega + 2E) + 16\sin(2\omega + 3E) - 3e\sin(2\omega + 4E) - 12eE\cos 2\omega\right) \tag{67}$$

$$\text{fun}_2^e = \frac{1}{120}\left(-15e\sin(4\omega + 2E) + 40\sin(4\omega + 3E) - 45e\sin(4\omega + 4E) + 24\sin(4\omega + 5E) - 5e\sin(4\omega + 6E)\right)$$

(68)

$$\text{fun}_3^e = \frac{1}{1120}\left(-70e\sin(6\omega + 4E) + 224\sin(6\omega + 5E) - 280e\sin(6\omega + 6E) + 160\sin(6\omega + 7E) - 35e\sin(6\omega + 8E)\right)$$

(69)

$$\text{fun}_4^e = \frac{1}{5040}\left(-210e\sin(8\omega + 6E) + 720\sin(8\omega + 7E) - 945e\sin(8\omega + 8E) + 560\sin(8\omega + 9E) - 126e\sin(8\omega + 10E)\right)$$

(70)

$$\text{fun}_0^i = \frac{1}{24}\left(\begin{array}{l} -3e\left(\frac{7}{\sqrt{1-e^2}} + 1\right)\sin E + 3\left(\frac{1+e^2}{\sqrt{1-e^2}} - 1\right)\sin 2E - e\left(\frac{1}{\sqrt{1-e^2}} - 1\right)\sin 3E \\ +3e\left(\frac{1}{\sqrt{1-e^2}} - 1\right)\sin(2\omega - E) - \frac{18e}{\sqrt{1-e^2}}\sin(2\omega + E) + 3\left(\frac{1+e^2}{\sqrt{1-e^2}} + 1\right)\sin(2\omega + 2E) - e\left(\frac{1}{\sqrt{1-e^2}} + 1\right)\sin(2\omega + 3E) \\ +6\left(\frac{1+e^2}{\sqrt{1-e^2}} + 1\right)E + 6\left(\frac{1+e^2}{\sqrt{1-e^2}} - 1\right)E\cos 2\omega \end{array}\right)$$

(71)

$$\mathrm{fun}_1^i=\frac{1}{240}\left(\begin{array}{c}\left(\begin{array}{c}-30e\cos(\omega-E)+30\cos(\omega+2E)-10e\cos(\omega+3E)\\+30e\cos(3\omega+E)-30\cos(3\omega+2E)+15\cos(3\omega+4E)-6e\cos(3\omega+5E)\end{array}\right)\sin\omega\\+\left(\begin{array}{c}30e\sin(\omega-E)+30\left(1+e^2\right)\sin(\omega+2E)-10e\sin(\omega+3E)\\-30e\sin(3\omega+E)+30\left(1+e^2\right)\sin(3\omega+2E)+15\left(1+e^2\right)\sin(3\omega+4E)-6e\sin(3\omega+5E)\\-180e\sin(\omega+E)-60e\sin(3\omega+3E)\end{array}\right)\frac{\cos\omega}{\sqrt{1-e^2}}\\+30\left(\frac{1+e^2}{\sqrt{1-e^2}}+1\right)E+30\left(\frac{1+e^2}{\sqrt{1-e^2}}-1\right)E\cos2\omega\end{array}\right)$$

(72)

$$\mathrm{fun}_2^i=\frac{1}{1680}\left(\begin{array}{c}\left(\begin{array}{c}210e\cos(3\omega+E)-210\cos(3\omega+2E)+105\cos(3\omega+4E)-42e\cos(3\omega+5E)\\+70e\cos(5\omega+3E)-105\cos(5\omega+4E)+70\cos(5\omega+6E)-30e\cos(5\omega+7E)\end{array}\right)\sin\omega\\+\left(\begin{array}{c}-210e\sin(3\omega+E)+210\left(1+e^2\right)\sin(3\omega+2E)+105\left(1+e^2\right)\sin(3\omega+4E)-42e\sin(3\omega+5E)\\-70e\sin(5\omega+3E)+105\left(1+e^2\right)\sin(5\omega+4E)+70\left(1+e^2\right)\sin(5\omega+6E)-30e\sin(5\omega+7E)\\-420e\sin(3\omega+3E)-252e\sin(5\omega+5E)\end{array}\right)\frac{\cos\omega}{\sqrt{1-e^2}}\end{array}\right)$$

(73)

$$\mathrm{fun}_3^i=\frac{1}{10080}\left(\begin{array}{c}\left(\begin{array}{c}420e\cos(5\omega+3E)-630\cos(5\omega+4E)+420\cos(5\omega+6E)-180e\cos(5\omega+7E)\\+252e\cos(7\omega+5E)-420\cos(7\omega+6E)+315\cos(7\omega+8E)-140e\cos(7\omega+9E)\end{array}\right)\sin\omega\\+\left(\begin{array}{c}-420e\sin(5\omega+3E)+630\left(1+e^2\right)\sin(5\omega+4E)+420\left(1+e^2\right)\sin(5\omega+6E)-180e\sin(5\omega+7E)\\-252e\sin(7\omega+5E)+420\left(1+e^2\right)\sin(7\omega+6E)+315\left(1+e^2\right)\sin(7\omega+8E)-140e\sin(7\omega+9E)\\-1512e\sin(5\omega+5E)-1080e\sin(7\omega+7E)\end{array}\right)\frac{\cos\omega}{\sqrt{1-e^2}}\end{array}\right)$$

(74)

$$\mathrm{fun}_4^i=\frac{1}{110880}\left(\begin{array}{c}\left(\begin{array}{c}2772e\cos(7\omega+5E)-4620\cos(7\omega+6E)+3465\cos(7\omega+8E)-1540e\cos(7\omega+9E)\\+1980e\cos(9\omega+7E)-3465\cos(9\omega+8E)+2772\cos(9\omega+10E)-1260e\cos(9\omega+11E)\end{array}\right)\sin\omega\\+\left(\begin{array}{c}-2772e\sin(7\omega+5E)+4620\left(1+e^2\right)\sin(7\omega+6E)+3465\left(1+e^2\right)\sin(7\omega+8E)-1540e\sin(7\omega+9E)\\-1980e\sin(9\omega+7E)+3465\left(1+e^2\right)\sin(9\omega+8E)+2772\left(1+e^2\right)\sin(9\omega+10E)-1260e\sin(9\omega+11E)\\-11880e\sin(7\omega+7E)-9240e\sin(9\omega+9E)\end{array}\right)\frac{\cos\omega}{\sqrt{1-e^2}}\end{array}\right)$$

(75)

$$\mathrm{fun}_0^\Omega=\frac{1}{24}\left(\begin{array}{c}-3e\left(\frac{5}{\sqrt{1-e^2}}-1\right)\cos E+3\left(\frac{1+e^2}{\sqrt{1-e^2}}-1\right)\cos2E-e\left(\frac{1}{\sqrt{1-e^2}}-1\right)\cos3E\\-3e\left(\frac{1}{\sqrt{1-e^2}}-1\right)\cos(2\omega-E)+\frac{18e}{\sqrt{1-e^2}}\cos(2\omega+E)-3\left(\frac{1+e^2}{\sqrt{1-e^2}}+1\right)\cos(2\omega+2E)+e\left(\frac{1}{\sqrt{1-e^2}}+1\right)\cos(2\omega+3E)\\+6\left(\frac{1+e^2}{\sqrt{1-e^2}}-1\right)E\sin2\omega\end{array}\right)$$

(76)

$$\mathrm{fun}_1^{\Omega}=\frac{1}{240}\left(\begin{array}{c}\begin{pmatrix}30e\cos(\omega-E)-30\cos(\omega+2E)+10e\cos(\omega+3E)\\-30e\cos(3\omega+E)+30\cos(3\omega+2E)-15\cos(3\omega+4E)+6e\cos(3\omega+5E)\end{pmatrix}\cos\omega\\+\left(\begin{array}{c}30e\sin(\omega-E)+30\left(1+e^2\right)\sin(\omega+2E)-10e\sin(\omega+3E)\\-30e\sin(3\omega+E)+30\left(1+e^2\right)\sin(3\omega+2E)+15\left(1+e^2\right)\sin(3\omega+4E)-6e\sin(3\omega+5E)\\-180e\sin(\omega+E)-60e\sin(3\omega+3E)\end{array}\right)\frac{\sin\omega}{\sqrt{1-e^2}}\\+30\left(\frac{1+e^2}{\sqrt{1-e^2}}-1\right)E\sin 2\omega\end{array}\right)$$

(77)

$$\mathrm{fun}_2^{\Omega}=\frac{1}{1680}\left(\begin{array}{c}\begin{pmatrix}-210e\cos(3\omega+E)+210\cos(3\omega+2E)-105\cos(3\omega+4E)+42e\cos(3\omega+5E)\\-70e\cos(5\omega+3E)+105\cos(5\omega+4E)-70\cos(5\omega+6E)+30e\cos(5\omega+7E)\end{pmatrix}\cos\omega\\+\left(\begin{array}{c}-210e\sin(3\omega+E)+210\left(1+e^2\right)\sin(3\omega+2E)+105\left(1+e^2\right)\sin(3\omega+4E)-42e\sin(3\omega+5E)\\-70e\sin(5\omega+3E)+105\left(1+e^2\right)\sin(5\omega+4E)+70\left(1+e^2\right)\sin(5\omega+6E)-30e\sin(5\omega+7E)\\-420e\sin(3\omega+3E)-252e\sin(5\omega+5E)\end{array}\right)\frac{\sin\omega}{\sqrt{1-e^2}}\end{array}\right)$$

(78)

$$\mathrm{fun}_3^{\Omega}=\frac{1}{10080}\left(\begin{array}{c}\begin{pmatrix}-420e\cos(5\omega+3E)+630\cos(5\omega+4E)-420\cos(5\omega+6E)+180e\cos(5\omega+7E)\\-252e\cos(7\omega+5E)+420\cos(7\omega+6E)-315\cos(7\omega+8E)+140e\cos(7\omega+9E)\end{pmatrix}\cos\omega\\+\left(\begin{array}{c}-420e\sin(5\omega+3E)+630\left(1+e^2\right)\sin(5\omega+4E)+420\left(1+e^2\right)\sin(5\omega+6E)-180e\sin(5\omega+7E)\\-252e\sin(7\omega+5E)+420\left(1+e^2\right)\sin(7\omega+6E)+315\left(1+e^2\right)\sin(7\omega+8E)-140e\sin(7\omega+9E)\\-1512e\sin(5\omega+5E)-1080e\sin(7\omega+7E)\end{array}\right)\frac{\sin\omega}{\sqrt{1-e^2}}\end{array}\right)$$

(79)

$$\mathrm{fun}_4^{\Omega}=\frac{1}{110880}\left(\begin{array}{c}\begin{pmatrix}-2772e\cos(7\omega+5E)+4620\cos(7\omega+6E)-3465\cos(7\omega+8E)+1540e\cos(7\omega+9E)\\-1980e\cos(9\omega+7E)+3465\cos(9\omega+8E)-2772\cos(9\omega+10E)+1260e\cos(9\omega+11E)\end{pmatrix}\cos\omega\\+\left(\begin{array}{c}-2772e\sin(7\omega+5E)+4620\left(1+e^2\right)\sin(7\omega+6E)+3465\left(1+e^2\right)\sin(7\omega+8E)-1540e\sin(7\omega+9E)\\-1980e\sin(9\omega+7E)+3465\left(1+e^2\right)\sin(9\omega+8E)+2772\left(1+e^2\right)\sin(9\omega+10E)-1260e\sin(9\omega+11E)\\-11880e\sin(7\omega+7E)-9240e\sin(9\omega+9E)\end{array}\right)\frac{\sin\omega}{\sqrt{1-e^2}}\end{array}\right)$$

(80)

$$\mathrm{fun}_0^{\omega}=\frac{1}{2}\left(-2\left(2-e^2\right)\cos E+e\cos^2 E\right)\qquad(81)$$

$$\mathrm{fun}_1^{\omega}=\frac{1}{48}\left(24\left(2-e^2\right)\cos(2\omega+E)-8\left(2-e^2\right)\cos(2\omega+3E)+3e\cos(2\omega+4E)+12eE\sin 2\omega\right)\qquad(82)$$

$$\mathrm{fun}_2^{\omega}=\frac{1}{120}\left(-15e\cos(4\omega+2E)+20\left(2-e^2\right)\cos(4\omega+3E)-12\left(2-e^2\right)\cos(4\omega+5E)+5e\cos(4\omega+6E)\right)$$

(83)

$$\mathrm{fun}_3^{\omega}=\frac{1}{1120}\left(-70e\cos(6\omega+4E)+112\left(2-e^2\right)\cos(6\omega+5E)-80\left(2-e^2\right)\cos(6\omega+7E)+35e\cos(6\omega+8E)\right)$$

(84)

$$\mathrm{fun}_4^{\varpi} = \frac{1}{2520}\left(-105e\cos(8\omega+6E)+180\left(2-e^2\right)\cos(8\omega+7E)-140\left(2-e^2\right)\cos(8\omega+9E)+63e\cos(8\omega+10E)\right) \tag{85}$$

## REFERENCES


[1] http://www.oneweb.world/#use [retrieved 07 June 2019].

[2] https://www.spacex.com/ [retrieved 07 June 2019].

[3] "OneWeb Minisatellite Constellation for Global Internet Service", https://directory.eoportal.org/web/eoportal/satellite-missions/content/-/article/oneweb [retrived 07 June 2019].

[4] Colombo C., Lücking C., McInnes C. R., "Orbital Dynamics of High Area-to-Mass Ratio Spacecraft with $J_2$ and Solar Radiation Pressure for Novel Earth Observation and Communication Services", *Acta Astronautica*, Vol. 81, No. 1, 2012, pp. 137-150. doi: 10.1016/j.actaastro.2012.07.009.

[5] Lücking C., Colombo C., McInnes C. R., "Solar Radiation Pressure-Augmented Deorbiting: Passive End-of-Life Disposal from High-Altitude Orbits", *Journal of Spacecraft and Rockets*, v. 50, n. 6, pp. 1256-1267, Dec. 2013, doi: abs/10.2514/1.A32478, ISSN 0022-4650.

[6] Lücking C., Colombo C., McInnes C. R., "A Passive Satellite Deorbiting Strategy for Medium Earth Orbit Using Solar Radiation Pressure and the J2 Effect", Acta Astronautica, Vol. 77, 2012, pp. 197-206. doi: 10.1016/j.actaastro.2012.03.026.

[7] Colombo, C., and de Bras de Fer, T., "Assessment of Passive and Active Solar Sailing Strategies for End-of-Life Re-Entry," *67th International Astronautical Congress*, Guadalajara, Mexico: 2016, IAC-16-A6.4.4.

[8] Alessi, E. M., Schettino, G., Rossi, A., and Valsecchi, G. B., "Solar Radiation Pressure Resonances in Low Earth Orbits," *Monthly Notices of the Royal Astronomical Society*, vol. 473, 2017, pp. 2407–2414.

[9] Alessi, E. M., and Colombo, C., "Dynamical System Description of the Solar Radiation Pressure and J2 Phase Space for End-of-Life Design and Frozen Orbit Design," *69th International Astronautical Congress*, 2018, IAC-18,A6,10-C1.7,11,x45107.

[10] Huang, S., Colombo, C., Alessi, E. M., and Hou, Z., "Large Constellation De-Orbiting With Low-Thrust Propulsion," *29th AAS/AIAA Space Flight Mechanics Meeting*, Ka'anapali, HI: 2019, AAS 19-480.

[11] Edelbaum, T. N., "Propulsion Requirements for Controllable Satellites," *ARS Semi-Annual Meeting*, Los Angeles, Calif: 1960, pp. 1079–1089.

[12] Kluever, C. A., and Oleson, S. R., "Direct Approach for Computing Near-Optimal Low-Thrust Earth-Orbit Transfers," *Journal of Spacecraft and Rockets*, vol. 35, 1998, pp. 509–515.

[13] Gao, Y., "Near-Optimal Very Low-Thrust Earth-Orbit Transfers and Guidance Schemes," *Journal of Guidance, Control, and Dynamics*, vol. 30, 2007, pp. 529–539.

[14] Pollard, J. E., "Simplified Approach for Assessment of Low-Thrust Elliptical Orbit Transfers," *25th International Electric Propulsion Conference*, Cleveland, Ohio: 1997, pp. 979–986.

[15] Neta, B., and Vallado, D., On Satellite Umbra/Penumbra Entry and Exit Positions, 1997.

[16] Battin, R. H., An Introduction to the Mathematics and Methods of Astrodynamics, 1999.

[17] *SpaceX Non-Geostationary Satellite System - Attachment A: Technical Information to Supplement Schedule S*, 2016.

[18] Larson, W. J., and Wertz, J. R., Space Mission Analysis and Design, 1999.

[19] Lang, T. J., "A Comparison of Satellite Constellations for Continuous Global Coverage," *Mission Design & Implementation of Satellite Constellations*, Toulouse, France: Springer, Dodrecht, 1998, pp. 51–62.

[20] Lang, T. J., "Low Earth Orbit Satellite Constellations for Continuous Coverage of the Mid-Latitudes," *AIAA/AAS Astrodynamics Conference*, San Diego, CA: 1996, pp. 595–607.

[21] Rossi, A., Colombo, C., Tsiganis, K., et al., "ReDSHIFT: A Global Approach to Space Debris Mitigation", *Aerospace*, vol. 5(2), 64, 2018.

[22] Letterio, F., Alessi, E. M., Gkolias, I., et al., "RedSHIFT Software Tool for the Design and Computation of Mission End-of-Life-Disposal", *7th International Conference on Astrodynamics Tools and Techniques (ICATT)*, 6-9 Nov. 2018, DLR Oberpfaffenhofen, Germany.

[23] Schettino, G., Alessi, E. M., Rossi, A., Valsecchi, G. B., "Exploiting Dynamical Perturbations for the End-of-Life Disposal of Spacecraft in LEO", *Astronomy and Computing*, Vol. 27, 2019, pp. 1-10.